

A spectroscopically confirmed $z = 1.327$ galaxy-scale deflector magnifying a $z \sim 8$ Lyman-Break galaxy in the Brightest of Reionizing Galaxies survey

R. L. Barone-Nugent,^{1,*} A. Sonnenfeld,² J. S. B. Wyithe,¹ M. Trenti,¹ T. Treu,² K. B. Schmidt,³ P. A. Oesch,⁴ L. Bradley,⁵ and T. Puzia⁶

¹ School of Physics, University of Melbourne, Parkville 3010, VIC, Australia

² Department of Physics and Astronomy, University of California, Los Angeles, CA 90095-1547, USA

³ Department of Physics, University of California, Santa Barbara, CA 93106-9530, USA

⁴ Yale Center for Astronomy and Astrophysics, Yale University, New Haven, CT 06520, USA

⁵ Space Telescope Science Institute, 3700 San Martin Drive, Baltimore, MD 21218 USA

⁶ Institute of Astrophysics, Pontificia Universidad Catolica de Chile, Avenida Vicuna Mackenna 4860, Macul, 7820436, Santiago, Chile

*Email: robertbn@student.unimelb.edu.au

31 October 2018

ABSTRACT

We present a detailed analysis of an individual case of gravitational lensing of a $z \sim 8$ Lyman-Break galaxy (LBG) in a blank field, identified in Hubble Space Telescope imaging obtained as part of the Brightest of Reionizing Galaxies survey. To investigate the close proximity of the bright ($m_{AB} = 25.8$) Y_{098} -dropout to a small group of foreground galaxies, we obtained deep spectroscopy of the dropout and two foreground galaxies using VLT/X-Shooter. We detect H- α , H- β , [OIII] and [OII] emission in the brightest two foreground galaxies (unresolved at the natural seeing of 0.8 arcsec), placing the pair at $z = 1.327$. We can rule out emission lines contributing all of the observed broadband flux in H_{160} band at 70σ , allowing us to exclude the $z \sim 8$ candidate as a low redshift interloper with broadband photometry dominated by strong emission lines. The foreground galaxy pair lies at the peak of the luminosity, redshift and separation distributions for deflectors of strongly lensed $z \sim 8$ objects, and we make a marginal detection of a demagnified secondary image in the deepest (J_{125}) filter. We show that the configuration can be accurately modelled by a singular isothermal ellipsoidal deflector and a Sérsic source magnified by a factor of $\mu = 4.3 \pm 0.2$. The reconstructed source in the best-fitting model is consistent with luminosities and morphologies of $z \sim 8$ LBGs in the literature. The lens model yields a group mass of $9.62 \pm 0.31 \times 10^{11} M_{\odot}$ and a stellar mass-to-light ratio for the brightest deflector galaxy of $M_{*}/L_B = 2.3_{-0.6}^{+0.8} M_{\odot}/L_{\odot}$ within its effective radius. The foreground galaxies' redshifts would make this one of the few strong lensing deflectors discovered at $z > 1$. Deeper imaging would allow for confirmation of the existence of the secondary image and elongation in the primary image, verifying multiple imaging and producing more robust estimations of the image magnifications.

Key words: galaxies: high-redshift — cosmology: observations — gravitational lensing: strong — galaxies: luminosity function

1 INTRODUCTION

The epoch of reionisation at redshift $z \sim 7 - 12$ (Komatsu et al. 2010; Shull et al. 2012; Ade et al. 2013) is a key period in the evolution of the Universe when the first galaxies formed and reionised the neutral Hydrogen in the intergalactic medium (IGM). Due to the absorption of emitted photons with energies high enough to ionise neutral Hydrogen, the spectra of these early galaxies have highly

attenuated regions bluer than the Lyman-alpha break at 1216\AA , enabling their identification from broad band imaging with the Lyman-break, or ‘dropout’, technique (Steidel et al. 1996; Giavalisco 2002). This technique has been used successfully to build large galaxy samples out to $z \sim 8$, with sources selected using observations from both ground and space based observatories (e.g. Bouwens et al. 2015; Finkelstein et al. 2014; Schmidt et al. 2014; Bradley

et al. 2012; McLure et al. 2013).

These new observations have opened the possibility of quantifying and studying the galaxy luminosity function during the epoch of reionisation as well as its evolution with redshift (Khochfar et al. 2007; Bouwens et al. 2008; Castellano et al. 2010; Trenti et al. 2010; Bouwens et al. 2011; Finkelstein et al. 2012; Bradley et al. 2012; Oesch et al. 2012; Schenker et al. 2013; Robertson et al. 2013; McLure et al. 2013; Finkelstein et al. 2014; Schmidt et al. 2014; Bouwens et al. 2015; Robertson et al. 2015). Measurement of the luminosity function is a key requirement for understanding the production of ionising photons at high redshift, which completes hydrogen reionisation. In this context, it is of fundamental importance to discriminate between intrinsic evolution of the galaxy luminosity function and observational selection effects.

One possible effect is gravitational lensing magnification bias (e.g., Wallington & Narayan 1993). While the fraction of random lines of sight at $z \gtrsim 6$ that are strongly gravitationally lensed by massive foreground galaxies is around ~ 0.5 per cent (Barkana & Loeb 2000; Comerford et al. 2002; Wyithe et al. 2011; Barone-Nugent et al. 2015; Mason et al. 2015), the steep nature of the high redshift luminosity function results in observationally bright Lyman-Break galaxies (LBGs) having an excess likelihood of having been gravitationally lensed (Wyithe et al. 2011; Fialkov & Loeb 2015). In general, magnification bias depends on the slope of the luminosity function of the source galaxies: steeper luminosity functions yield more lensed sources because the loss in solid angle is compensated by the steep rise in number counts at deeper flux limits. Therefore, this effect becomes especially important for the bright end of the galaxy luminosity function ($L > L_*$), where L_* is the “knee” of the luminosity function in the Schechter parameterization, $\phi(L)dL = \phi_*(L/L_*)^\alpha \exp^{-(L/L_*)} d(L/L_*)$. In Barone-Nugent et al. (2015) we showed that magnification bias exists in LBG surveys at $z \gtrsim 4$, and becomes a significant factor in surveys of LBGs at $z \gtrsim 7$, with ~ 10 per cent of LBGs brighter than L_* strongly-lensed in fields without massive structures such as the Hubble eXtreme Deep Field (XDF Illingworth et al. 2013), and Cosmic Assembly Near-infrared Deep Extragalactic Legacy Survey fields (CANDELS Grogin et al. 2011; Koekemoer et al. 2011).

The results in Barone-Nugent et al. (2015) confirm the prediction of Wyithe et al. (2011) that ~ 10 per cent of $z \sim 8$ LBGs in a survey with a flux limit around M_* , such as the Brightest of Reionizing Galaxies (BoRG) WFC3 HST survey (Trenti et al. 2012; Bradley et al. 2012), could be strongly lensed. Hence the BoRG survey offers the perfect dataset to extend the findings of Barone-Nugent et al. (2015). In fact, an analysis of the BoRG survey by Mason et al. (2015) found that 3 – 15 per cent of LBGs in the BoRG fields are expected to be strongly lensed, depending on the specific flux limit of each field. They also investigated individual $z \sim 8$ candidates in the BoRG survey and found one good candidate for strong gravitational lensing, having an estimated magnification of $\mu = 2.02 \pm 0.52$. They also identified a further three candidates with lower magnifications of $\mu = 1.80 \pm 0.33$, $\mu = 1.54 \pm 0.62$ and $\mu = 1.47 \pm 0.30$.

The relatively small number of $z \sim 8$ candidates in the BoRG survey do not allow a statistical approach, such as

that undertaken by Barone-Nugent et al. (2015), to detect evidence of gravitational lensing. In this paper, we adopt a direct approach to search for evidence of gravitational lensing by looking at individual LBGs. We only consider the highest signal-to-noise (S/N) LBGs in the BoRG sample, which includes 10 candidates detected at $S/N \geq 8\sigma$ and $m \lesssim 27$ ($\approx M_*$ at $z \sim 8$). The results from Barone-Nugent et al. (2015) and Mason et al. (2015) imply that ≈ 1 of these LBGs should be strongly gravitationally lensed. We inspected these 10 LBGs searching for potential gravitationally lensed configurations, and find one $z \sim 8$ candidate in close projection to a foreground group of galaxies.

This paper is structured as follows; We discuss the data, photometry and spectroscopy in Section 2. In Section 3 we introduce the Markov-Chain Monte Carlo (MCMC) method that we have applied to investigate the lensing hypothesis, as well as the MCMC results. In Section 4 we compare the inferred $z \sim 8$ source properties to those in the literature. In Section 5 we investigate the properties of the deflector. We discuss the evidence for lensing in Section 6, and we conclude in Section 7. Throughout this paper we assume a Λ CDM cosmology of $\Omega_M = 0.27$, $\Omega_\Lambda = 0.73$ and $H_0 = 70 \text{ km s}^{-1} \text{ Mpc}^{-1}$. We quote magnitudes in the AB system (Oke & Gunn 1983). We refer to the F600LP, F098M, F125W and F160W HST filters as V_{600} , Y_{098} , J_{125} and H_{160} .

2 THE SEARCH FOR GRAVITATIONAL LENSING IN THE BRIGHTEST OF REIONIZING GALAXIES SURVEY

2.1 The BoRG survey

The BoRG survey is a Hubble Wide-Field Camera 3 (WFC3) large, multi-year pure-parallel program aimed at identifying galaxy candidates at $z \gtrsim 7.5$ from their colors based on the Lyman-break technique (Steidel et al. 1996). Until recently, the main focus of BoRG has been identification of galaxies at $z \sim 8$ as Y-band dropouts, while ongoing observations (cycle 22; #13767 PI Trenti) are optimized for selecting $z \sim 8 - 9$ candidates.

In this work, we use data from observations acquired before cycle 22 of the BoRG program. The core of this earlier dataset is based on WFC3 imaging in four filters (V_{600} , Y_{098} , J_{125} , H_{160}) obtained as part of HST programs #11700 and #12572 (PI Trenti), complemented by archival data with a similar observational design and the same infrared filters, but with F600LP substituting F606W (HST program #11702, PI Yan, Yan et al. 2011). A full description of the survey and of its findings is reported by Trenti et al. (2011, 2012), Bradley et al. (2012) and Schmidt et al. (2014). To summarize, the most recent comprehensive data release of the BoRG survey yielded $n = 38$ $z \sim 8$ LBG candidates identified as Y_{098} -dropouts with J_{125} magnitudes between 25.5 and 27.6 mag (Schmidt et al. 2014). These candidates were obtained by analyzing data over a total area of 350 arcmin² divided in 71 independent lines of sight.

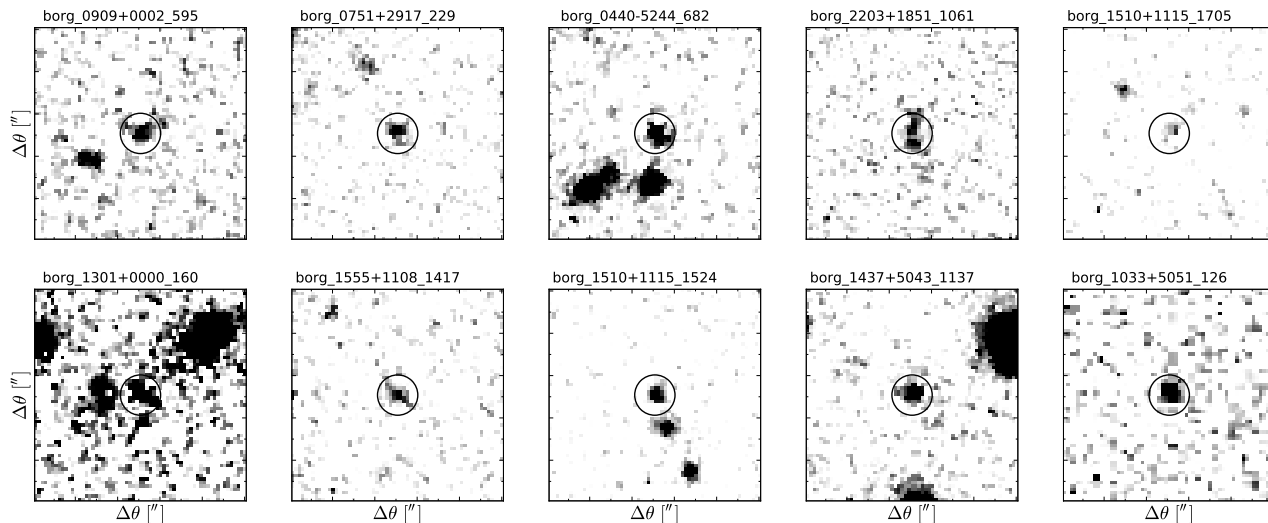


Figure 1. The 10 8σ $z \sim 8$ LBG candidates identified in the BoRG survey. The cutouts are 5 arcsec on each side, which is the characteristic scale for galaxy-galaxy lensing (Barone-Nugent et al. 2015), and shown in the J_{125} band. Seven of the 10 candidates are ruled out as being strongly gravitationally lensed due to the absence of foreground objects along the line of sight. The object borg_1301+0000.160 appears nearby a bright foreground galaxy, and Mason et al. (2015) assess its magnification to be $\mu = 1.47 \pm 0.30$. The object borg_1437+5043.1137 appears 2.6 arcsec from a bright foreground at $z_{phot} = 1.4$. Using the framework of Barone-Nugent et al. (2015), we assess this object’s magnification to be $\mu = 1.3 \pm 0.2$ and for it to have a 5 per cent chance of being strongly lensed. Neither of these configurations display obvious secondary images, which is the key criterion for constraining strong lensing. The object borg_0440-5244.682 is in close proximity to a group of three foreground galaxies, around which a candidate secondary image is identified.

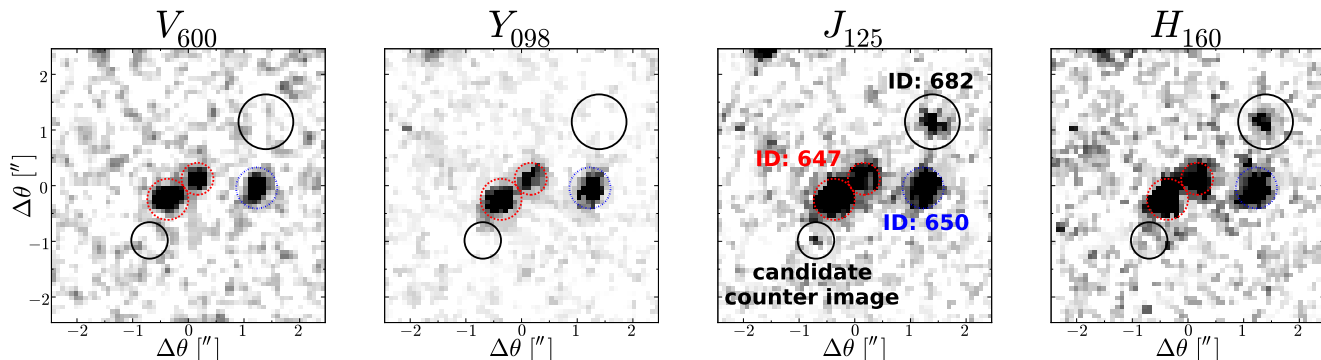


Figure 2. Postage stamp images of the candidate lensed $z \sim 8$ galaxy in field BoRG_0440-5244 in the four HST/WFC3 filters (left to right: V_{600} , Y_{098} , J_{125} , H_{160}). The two central foreground galaxies (ID: 647) are circled in red (dashed) and the third foreground galaxy (ID: 650) is circled in blue (dash-dotted). The location of the Y_{098} -dropout galaxy is marked by the larger black circle (solid), and the possible faint counter image on the opposite side of the lens is indicated by the smaller black circle (solid). The images are 5.0 arcsec on each side. All cutouts are shown on the same contrast scale.

2.2 Search for a candidate strongly lensed $z \sim 8$ LBG

The large number of independent fields in BoRG results in a sample essentially unaffected by large-scale structure uncertainty (Trenti & Stiavelli 2008), and includes a variety of different environments in terms of line-of-sight structure, representing an ideal dataset to quantify magnification bias in a different manner to that used by Barone-Nugent et al. (2015) and Mason et al. (2015). To search for evidence of large magnifications, we have visually inspected the regions surrounding the 10 sources detected with a $S/N \geq 8\sigma$ in the BoRG survey, all of which have $m_{J_{125}} < 27.0$. We investigate the highest S/N objects because they offer the best chance of identifying direct evidence of strong lensing in the event that they have been significantly

magnified. The indications of strong gravitational lensing that we inspect for are proximity of the dropout to bright foreground objects, and secondary images with similar colours to the dropout. Cutouts of the 10 candidates in the J_{125} band are shown in Fig. 1.

We identify one good candidate for being a strongly gravitationally lensed LBG at $z \sim 8$ (borg_0440-5244.682 in the notation of Bradley et al. 2012), which appears very close in projection to a compact grouping of three foreground galaxies (borg_0440-5244.647, which consists of two objects, and borg_0440-5244.650). Through visual inspection of the configuration, we identify a faint ($S/N \sim 2$) possible counter image, which appears in the deepest band, J_{125} , and is located immediately below the foreground galaxies opposite the location of the dropout. The location

and flux relative to the brighter image is consistent with gravitational lensing theory, which predicts secondary images to appear demagnified on the opposite side of the deflector, and at a smaller separation from the deflector than the brighter image. In fact, a strikingly similar gravitational lensing configuration has been observed (Wong et al. 2014, see fig. 3) with almost identical relative image positions, magnifications and flux ratio, albeit with a lower redshift source and smaller deflection angles.

The proximity to multiple bright foreground galaxies and identification of a possible secondary image with similar colours to the dropout makes borg_0440-5244.682 a good candidate to be magnified significantly, warranting further investigation. Postage stamp images of the dropout and foreground galaxies in the single optical and three near-IR filters of the BoRG survey are presented in Fig. 2, where the objects are labelled in the J_{125} panel.

2.3 Photometry of the dropout and foreground objects

The candidate $z \sim 8$ galaxy, borg_0440-5244.682, was identified in the BoRG field borg_0440-5244. Identification of $z \sim 8$ dropouts is made according to strict colour selection. In general, $z \gtrsim 7.5$ galaxies are identified due to a strong break between the Y_{098} and J_{125} filters, a blue or flat $J_{125} - H_{160}$ colour and a non-detection in the optical V_{600} band. The selection criteria requires,

$$\begin{aligned} S/N_{V_{600}} &< 1.5 \\ (Y_{098} - J_{125}) &> 1.75 \\ (J_{125} - H_{160}) &< 0.02 + 0.15[(Y_{098} - J_{125}) - 1.75]. \end{aligned}$$

The conservative non-detection limit of 1.5σ in the V_{600} filter is crucial in producing a clean $z \sim 8$ sample (Bouwens et al. 2011). The photometry presented by Bradley et al. (2012) of the candidates analyzed here gives a J_{125} magnitude of 25.9 ± 0.1 mag, a $Y_{098} - J_{125}$ residual of > 2.1 mag, and S/N after sky subtraction in V_{600} , Y_{098} , J_{125} and H_{160} of $-0.8, -0.5, 9.1$ and 5.7 , respectively. We find a J_{125} ellipticity for the dropout of $\epsilon = 0.4 \pm 0.1$ tangential to the direction of the largest of the proposed lensing galaxies. The J_{125} half-light radius of the dropout was measured, using **SExtractor**, to be 0.21 arcsec (1.1 kpc at $z \sim 8$; not corrected for point spread function (PSF) broadening).

The two brighter foreground objects are identified as a single blended source (borg_0440-5244.647) with $m_{J_{125}} = 23.41 \pm 0.02$ mag in the BoRG **SExtractor** catalogue. We performed fixed aperture photometry on the individual galaxies of borg_0440-5244.647 and found the brighter galaxy to be 1.3 – 1.5 mag brighter than the fainter galaxy in each of the filters, making the colours of the two galaxies essentially identical. The galaxy borg_0440-5244.650, has $m_{J_{125}} \sim 24.58 \pm 0.14$ mag. The photometry of all objects is summarised in Table 1.

2.4 Photometry of the candidate counter image

In addition to the photometry already carried out by Bradley et al. (2012), we perform aperture photometry in

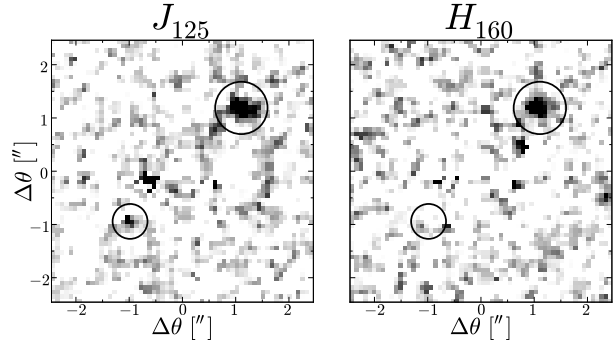


Figure 3. Normalized residuals for the subtractions of the PSF-matched Y_{098} image from the J_{125} image (left) and H_{160} image (right). The images are 5.0 arcsec on each side. There remains some residual of the deflector galaxy cores due to the varying light profiles of the galaxies between filters. There is a marginal detection of the counter image ($S/N \sim 2$) in J_{125} . As expected, the counter image is undetected in the H_{160} filter. The primary and candidate counter images are both circled in black.

IRAF on the primary and counter images to determine their flux ratio and the counter image's $Y_{098} - J_{125}$ and $V_{600} - J_{125}$ colours. To minimize contamination of the counter image photometry by the lensing group, we operate on a version of the J_{125} and H_{160} images where we subtracted a scaled and PSF-matched version of the Y_{098} data, where the $z \sim 8$ candidate has dropped out. For this, we use **ISIS2.2** (Alard 2000) to produce a convolution kernel between the images in the different bands and to match the PSFs. There is some residual in the subtracted images due to the foreground galaxies having intrinsically different profiles between filters. The galaxies on the whole, though, are adequately subtracted, and the residuals do not affect the photometry at the image positions. The subtracted images are shown in Fig. 3.

Photometry is performed in a 4 pixel circular aperture (0.32 arcsec). In J_{125} , the integrated flux in the primary image is $1.54 \pm 0.18 \times 10^{-30}$ erg cm $^{-2}$ s $^{-1}$ Hz $^{-1}$ (consistent with the $S/N = 9.1$ determination in Bradley et al. 2012), and the flux in the counter image is $3.21 \pm 1.72 \times 10^{-31}$ erg cm $^{-2}$ s $^{-1}$ Hz $^{-1}$. The uncertainty includes both Poisson noise and background. This gives a flux ratio of 4.8 ± 2.6 , where the large error propagates from the low S/N of the counter image.

We measure a $Y_{098} - J_{125}$ colour redder than 1.2 mag and a $V_{600} - J_{125}$ colour redder than 0.5 mag for the counter image. When the Y_{098} and V_{600} images are stacked, the $(Y_{098} + V_{600}) - J_{125}$ colour is redder than 1.4 mag. While BoRG is not designed to detect such faint objects, and neither of these colours satisfy the formal BoRG criteria for $z \sim 8$ LBG selection, the colours are consistent with both the brighter image, and the source being at $z \sim 8$ but beyond the 5σ limiting flux of this field.

We do not detect a signal at the location of the counter image in the H_{160} image, however this is not surprising as the flux ratio between the primary and counter image is measured in J_{125} to be 4.8 ± 2.6 , and the H_{160} primary image is detected at 5.7σ , hence we only expect the H_{160} counter image to be undetected ($S/N = 1.2 \pm 0.7$). Inspection of the individual flat-fielded files in J_{125} does not suggest that the

ID	V_{600}	Y_{098}	J_{125}	H_{160}
682	> 28.26	> 28.15	25.92 ± 0.14	25.75 ± 0.19
647	24.20 ± 0.07	23.87 ± 0.03	23.41 ± 0.02	23.49 ± 0.04
650	25.17 ± 0.13	24.87 ± 0.05	24.58 ± 0.14	24.31 ± 0.31

Table 1. The photometry for the primary dropout (ID: 682), the main lensing group (ID: 647) and a nearby galaxy (ID: 650) which is potentially part of the group. The main lensing group (647) has a spectroscopically confirmed redshift of $z = 1.327$. The photometric redshift probability distribution of the third object (650) is extended, however it has a non-negligible probability of residing at the same redshift as the central galaxies.

faint candidate counter image is a detector artifact.

The non-detection in H_{160} is taken into account in our Markov-Chain Monte Carlo analysis (Section 3), as both bands are fitted simultaneously.

2.5 Spectroscopy of the central foreground galaxies and dropout

The source and foreground galaxy configuration and image flux ratios outlined in the previous sections and Fig. 2 present the exciting possibility that this system is a $z \sim 8$ galaxy gravitationally lensed by a foreground galaxy group. In order to further strengthen this interpretation, we obtained spectroscopic observations of the foreground galaxy group and $z \sim 8$ LBG candidate. The goals of the spectroscopic measurements of the system are two-fold; The first goal was to obtain spectroscopic redshifts for the two foreground galaxies (ID: 647), and the second goal was to either identify emission lines, such as Lyman-alpha emission, at the location of the $z \sim 8$ LBG candidate (ID: 682), or use the lack of emission lines to constrain its redshift in conjunction with its photometric colours (e.g. Treu et al. 2013).

In order to obtain these measurements, we carried out VLT/X-Shooter spectroscopic observations in visitor mode on August 13-15, 2013 (program #091.A-0053, PI Puzia). Observing conditions were excellent with seeing in the range 0.6–0.9 arcsec. The X-Shooter long slit (11 arcsec) was positioned to cover both the central pair of foreground deflectors and the Y-dropout. X-Shooter provides an uninterrupted wavelength coverage in the range $300 \text{ nm} < \lambda < 2480 \text{ nm}$, allowing us to characterise emission lines both from the deflector and the dropouts with a single observation. A total exposure time of 6 hours (3 hours on target) was achieved on the source. Telluric standard stars were observed for calibration purposes throughout the duration of the observations. The data was then reduced using the European Southern Observatory (ESO) X-Shooter pipeline v.2.5.2 (Modigliani et al. 2010) and the Gasgano data file organizer developed by ESO.

2.5.1 Emission lines from the foreground galaxies

We search for emission lines at the location of the two central foreground galaxies to determine their redshifts. The two galaxies have a separation of 0.7 arcsec, and the seeing of the observations was 0.6–0.9 arcsec, therefore the

two galaxies are unresolved in the spectrum. We identify the redshifted hydrogen-alpha 6563\AA , hydrogen-beta 4861\AA , [OIII] 5007\AA and 4959\AA doublet and the [OII] 3726\AA and 3729\AA doublet emission lines at the location of the two foreground galaxies. The two-dimensional (2D) spectrum of the hydrogen-alpha and [OIII] doublet emission lines are shown in Fig. 4. The observed emission lines unambiguously places the foreground galaxy pair at $z = 1.327$, which supports the strong gravitational lensing hypothesis. This redshift is at the peak of the redshift distribution for the deflectors of $z \sim 7$ -8 LBGs (Barone-Nugent et al. 2015).

It should be noted that there is a chance that the emission lines are coming only from the brighter foreground galaxy. However, the colours of the two central galaxies are virtually identical and no emission lines are observed at the location of the fainter galaxy elsewhere in the spectrum, leading to the likely possibility that the two galaxies are indeed a close pair at $z = 1.327$.

2.5.2 Constraints on the redshifts of the LBG

Spectroscopic confirmation of high redshift galaxies has been very difficult in the past, hence using gravitationally lensed LBGs provides the best opportunity to probe intrinsically fainter sources at high redshift. The $z \sim 8$ candidate LBG was included in our spectrum in order to search for the Lyman-alpha emission line. The X-Shooter wavelength coverage would allow detection of the Lyman-alpha line, from a Lyman-alpha emitter at $z \gtrsim 7$, as well as other emission lines such as CIII] and CIV. However we do not detect the Lyman-alpha line in the spectrum, nor do we detect any other emission lines. For an LBG residing at $7.6 \lesssim z \lesssim 8.8$ (the redshift where there is a non-negligible probability density for this LBG), we show the 2D spectrum of the Y_{098} dropout at the wavelengths where Lyman-alpha, CIII] and CIV could conceivably appear in Fig. 5. We place upper limits on the equivalent widths of these lines in Section 2.5.3.

Despite the lack of visible emission lines, the spectrum of the LBG candidate is nevertheless useful for constraining the strong lensing hypothesis since we can rule out the possibility of the source being a strong emission line contaminant. We do not observe any emission lines at the location of the dropout down to the sensitivity limit of the our spectroscopic observations. While this prevents us from achieving spectroscopic confirmation, the non-detection of emission lines is important to exclude the most significant class of contaminants in samples of high redshift LBGs. These contaminants are objects with a very weak continuum and very strong hydrogen-alpha, hydrogen-beta and [OIII] emission located at $1.3 \lesssim z \lesssim 1.7$. Such galaxies could exhibit colours similar to those observed in the $z \sim 8$ candidate of this paper (Atek et al. 2011).

We consider the noise levels of the dropout spectrum to place limits on the contribution to the observed broadband flux from emission lines. The integrated line flux at $\lambda \approx 1.6 \mu\text{m}$ required to produce a broadband flux of $m_{H_{160}} = 25.75 \text{ mag}$ is $7.8 \times 10^{-17} \text{ erg cm}^{-2} \text{ s}^{-1}$. Assuming a simple model of an emission line with a width of 10\AA , the required flux density to account for all of the broadband magnitude is $7.8 \times 10^{-18} \text{ erg cm}^{-2} \text{ s}^{-1} \text{ \AA}^{-1}$. The median

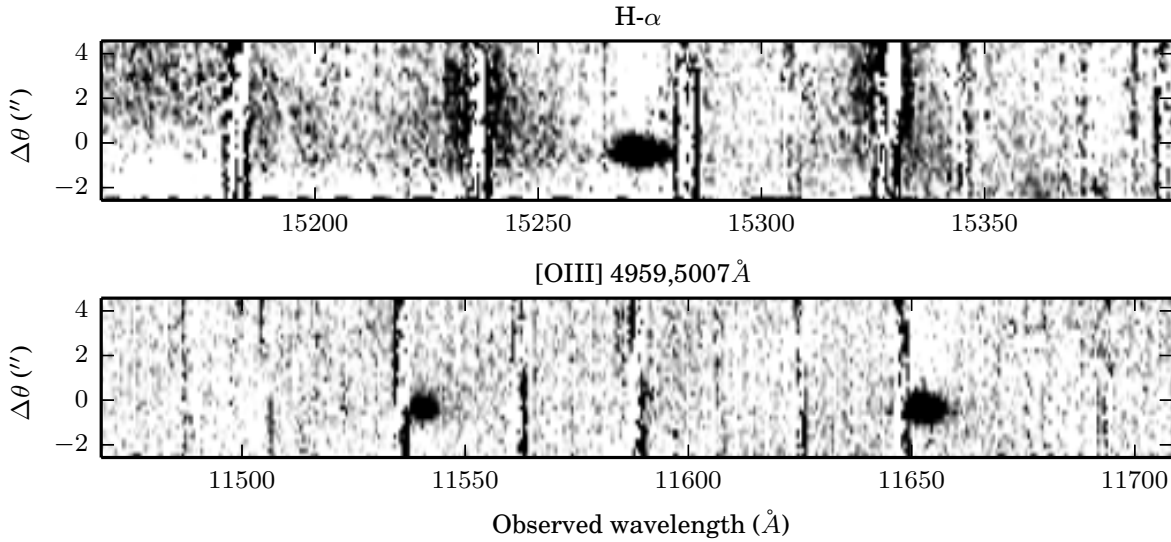


Figure 4. The cropped two-dimensional spectrum of the central deflector galaxies, obtained using X-Shooter on the VLT. Top: The hydrogen-alpha emission line, identified at $\lambda = 15272\text{\AA}$. Bottom: The [OIII] doublet emission lines, identified at $\lambda = 11540\text{\AA}$ and $\lambda = 11651\text{\AA}$. These emission lines provide a robust spectroscopic redshift of $z = 1.327$ for the deflector galaxies.

noise in the spectrum in the H_{160} band is $4.6 \times 10^{-19} \text{ erg cm}^{-2} \text{ s}^{-1} \text{ \AA}^{-1}$. This allows us to rule out the presence of an emission line contributing more than $m_{H_{160}} = 28.6$ at 5σ , and contributing all of the observed broadband flux of $m_{H_{160}} = 25.75$ mag at 70σ . Similarly, the integrated line flux required to produce a broadband flux of $m_{J_{125}} = 25.92$ mag is $7.9 \times 10^{-17} \text{ erg cm}^{-2} \text{ s}^{-1}$, and the median noise level in the spectrum covering the J_{125} band is $1.0 \times 10^{-18} \text{ erg cm}^{-2} \text{ s}^{-1} \text{ \AA}^{-1}$. This allows us to rule out the presence of an emission line contributing more than $m_{J_{125}} = 27.9$ mag at 5σ , and contributing the all of the observed broadband flux of $m_{J_{125}} = 25.92$ mag at 30σ .

We calculate the likelihood that the emission lines are hidden behind sky lines or obscured by atmospheric absorption. We define the obscured part of the spectrum as the region where an emission line detected at 5σ at the median noise would be detected at less than 2σ . The percentage of the spectrum covering the broadband J_{125} and H_{160} filters obscured by sky lines or atmospheric absorption above the required level of emission lines is ~ 14 per cent. If the dropout resides at $1.3 \lesssim z \lesssim 1.7$, the likelihood that both the brighter [OIII] emission line and hydrogen-alpha line are obscured is 10 per cent. The likelihood that the hydrogen-alpha line and both of the [OIII] lines are obscured is 7 per cent.

We conclude through this simple analysis that emission lines from the dropout source can contribute at most ~ 20 per cent of the broadband flux in J_{125} and less than ~ 10 per cent in H_{160} , therefore excluding lower redshift solutions with a faint (undetected) continuum and broadband photometry dominated by strong emission lines with very high confidence.

As a consistency check, we compare the required luminosity of the emission lines in the case of the dropout being a low redshift interloper with the detected emission lines of the foreground galaxies. For emission lines to contribute the required flux in J_{125} and H_{160} for the dropout, they

would need to be as bright as the observed [OIII] 4959Å line from the foreground galaxy pair, and twice as bright as the observed hydrogen-beta line, both of which are detected with high confidence ($\gtrsim 10\sigma$).

2.5.3 Equivalent width constraints from the LBG spectrum

In addition to ruling out strong emission line interlopers, the absence of emission lines allows us to place upper limits on the equivalent widths of the Lyman-alpha, CIII] and CIV emission lines for this LBG. Each of these emission lines have been observed in spectra of LBGs at $z \gtrsim 6$ previously (Ono et al. 2011; Finkelstein et al. 2013; Oesch et al. 2015; Stark et al. 2015b,a).

We investigate the limits that can be placed on the equivalent width of Lyman-alpha emission. We do this by assuming a half-Gaussian model of the Lyman-alpha emission line profile with a full width at half maximum (FWHM) of 12\AA . We calculate the 5σ upper limit on the integrated line flux by considering the noise in the spectrum in the possible wavelength range of Lyman-alpha emission. The continuum flux density is computed from the broadband photometry. The result is a median 5σ upper limit of the rest-frame equivalent width of $\text{EW}_0(\text{Lyman-}\alpha) < 57\text{\AA}$. We quantify the chance that Lyman-alpha is obscured by sky lines or atmospheric absorption in the region where we expect Lyman-alpha to appear. The redshift distribution for the LBG is centred on $z = 8$, but there is a non-negligible probability density from $z \sim 7.6$ to $z \sim 8.8$. Using the range of wavelengths at which Lyman-alpha could appear, we calculate that the chance that it has been obscured to be 14 per cent.

We also constrain the equivalent width of CIII] and CIV emission lines. For these emission lines, we assume a Gaussian emission line profile model with a FWHM of 12\AA . We calculate the 5σ upper limit on the integrated

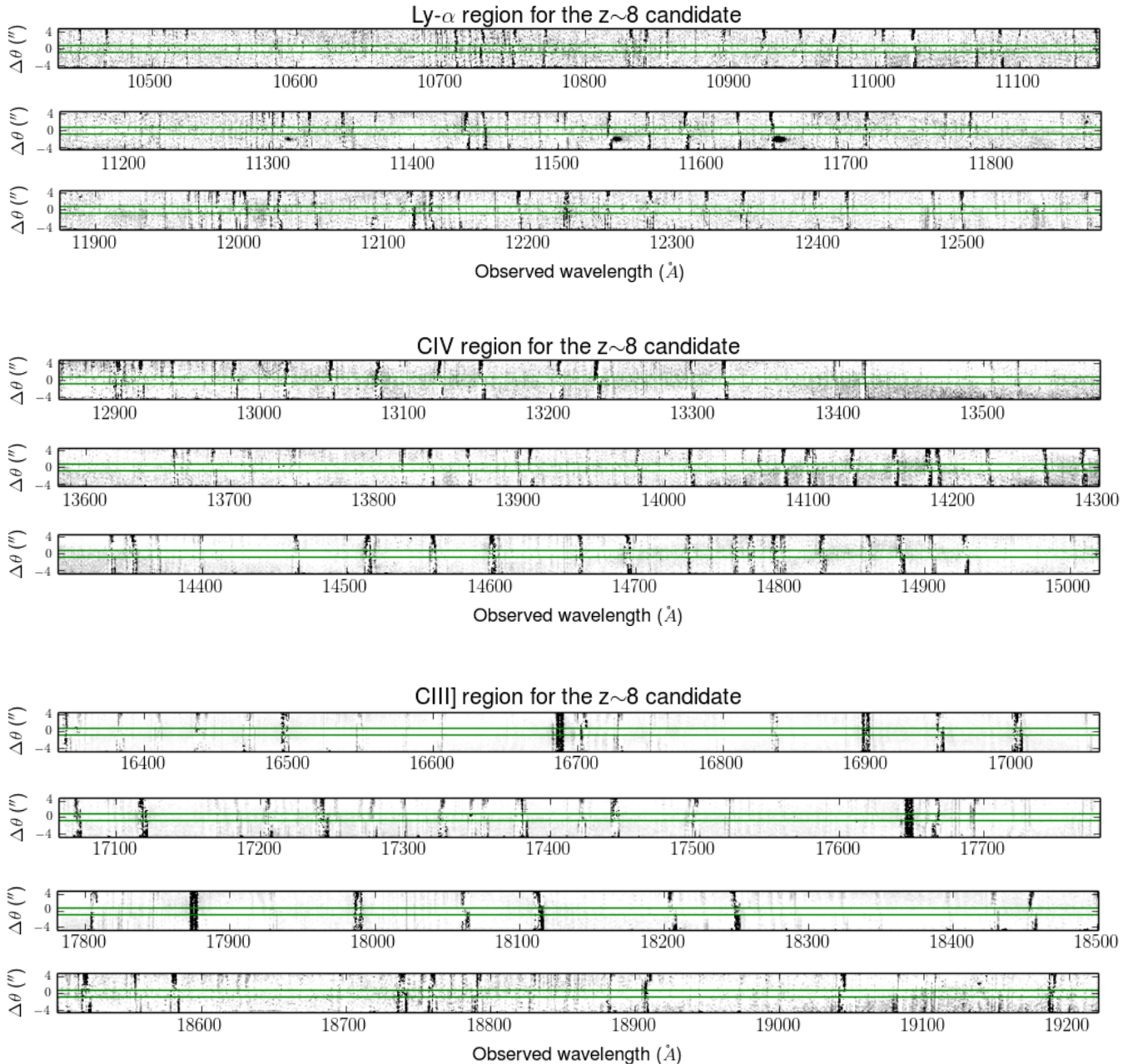


Figure 5. The regions of the 2D spectrum where the Lyman-alpha (1216Å, top), CIV (1548Å, middle), and CIII] (1909Å, bottom) emission lines could appear given the redshift distribution of the dropout. The portion of the spectrum covering the dropout falls within the green lines. No lines are detected at these wavelengths or elsewhere in the spectrum at the location of the dropout. We use these non-detections to rule out a major class of low-redshift interlopers, and constrain the equivalent widths of the Lyman-alpha, CIII] and CIV emission lines. The hydrogen-beta and [OIII] doublet emission lines from the central galaxy pair are visible in the Lyman-alpha detection region at 11312Å, 11540Å and 11651Å, respectively.

line flux by considering the noise in the spectrum in the possible wavelength range of CIII] and CIV emission. The continuum flux density is again calculated from the broadband photometry. The results are median 5σ upper limits for CIII] and CIV emission of $EW_0(\text{CIII])} < 25\text{\AA}$ and $EW_0(\text{CIV}) < 36\text{\AA}$, respectively. We quantify the chance of the CIII] and CIV lines being obscured by sky lines or due

to atmospheric absorption as 12 per cent in both cases.

2.5.4 Photometric redshift of the third foreground galaxy

The X-Shooter slit does not cover the third nearby foreground galaxy (ID: 650). To constrain the redshift of this source, we utilise the Bayesian photometric redshift code

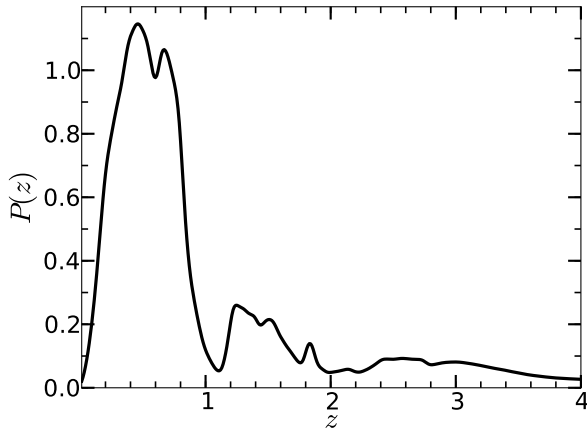


Figure 6. The redshift probability distribution function for the third foreground galaxy (ID: 650), obtained with the photometric redshift code BPZ using the Hubble Ultra Deep Field prior. The distribution is reasonably broad and peaks around $z = 0.2\text{--}0.4$, however a non-negligible peak at $z = 1.2\text{--}1.4$ leads to the distinct possibility that this object may also lie at the same redshift as the nearby $z = 1.327$ galaxies, forming a small group.

BPZ (Benitez 2000; Benítez et al. 2004; Coe et al. 2007; Benitez 2008). The photometric redshift distribution of this source is characterised by an extended probability distribution, peaking at $z \sim 0.3$. However, there is a non-negligible secondary peak in the likelihood distribution centred at $z = 1.3$, leading to the distinct possibility that this galaxy is at the same redshift as the central objects and the broad redshift distribution is simply an effect of photometric scatter. The photometric redshift distribution for this third galaxy is shown in Fig. 6.

The possibility that the third foreground galaxy is part of the group with the two galaxies at $z = 1.327$ supports a larger total dark matter mass of the deflector. However, the dark matter mass required for strong lensing in the lens modelling of the system (see Section 3) is not ruled out if this additional galaxy is not part of the group. In Section 3 we model the system with only a single mass distribution centred on the centre-of-light of the spectroscopically confirmed galaxy pair, thereby assuming it resides at the centre of the halo of the group.

3 MEASUREMENT OF LENS AND SOURCE PROPERTIES USING A MARKOV-CHAIN MONTE CARLO BAYESIAN INFERENCE

In this section, we model the observed configuration using a singular isothermal ellipsoid (SIE) mass distribution for the foreground group of galaxies, centred at the centre of light of the spectroscopically confirmed galaxy pair, and a Sérsic brightness profile for the source. We have implemented the Metropolis algorithm in a Markov-Chain Monte Carlo analysis to find the posterior probability distribution function of source and deflector parameters within a Bayesian framework.

Our deflector mass model consists of a SIE, which is a

generalisation of the singular isothermal sphere (SIS), and is a commonly used parametrisation of the mass distribution of a lensing galaxy (Keeton 2001a). The SIE provides an adequate representation of the mass distribution of massive elliptical galaxies (Kochanek 1995; Treu & Koopmans 2004; Koopmans et al. 2009; Treu 2010). We adopt the definitions of the Einstein radius, ellipticity and position angle as described by Keeton (2001a). The surface mass density, κ , in units of critical density, is defined by,

$$\kappa = \frac{1}{2} \frac{\theta_{ER}}{\sqrt{(1-\epsilon)x^2 + (1+\epsilon)y^2}}, \quad (1)$$

where θ_{ER} is the Einstein radius, $\epsilon = \frac{1-q^2}{1+q^2}$ and q is the axis ratio of the ellipsoid. According to this definition the Einstein radius is defined along the intermediate axis of the ellipsoid. The Einstein radius is then related to the velocity dispersion of the SIE profile by

$$\theta_{ER} = 4\pi \left(\frac{\sigma_*}{c}\right)^2 \frac{D_{LS}}{D_S}, \quad (2)$$

where σ_* is the line-of-sight stellar velocity dispersion, D_S is the angular diameter distance from the observer to the source and D_{LS} is the angular diameter distance from the deflector to the source. The centre of the SIE is fixed to coincide with the centre of light of the central galaxy pair. The deflector model therefore has three free parameters: Einstein radius (as a proxy for velocity dispersion/mass, and redshift), ellipticity and position angle.

We adopt the Sérsic profile (Sérsic 1963) for the source surface brightness distribution. The source is defined by six free parameters: the Sérsic index, the effective radius, flux, x -position, y -position, ellipticity and position angle. This gives a total of 10 parameters for the deflector-source gravitational lens model.

3.1 The MCMC method and code

We wrote an MCMC sampler in Python using the Metropolis algorithm. The code compares the BoRG data with surface brightness models of the image plane produced using GRAVLENS (Keeton 2001b).

The code follows a standard MCMC process. The log-likelihood is $\frac{1}{2}\chi^2$, where $\chi^2 = \sum \left(\frac{\text{model}_i - \text{data}_i}{\sigma_i}\right)^2$. The data are the WFC3 data in H_{160} and J_{125} and the model is the PSF-convolved image plane. We use uniform priors on all parameters. As lensing is achromatic, the only difference between the H_{160} model and the J_{125} model comes from the PSFs and the noise model. Hence, the log-likelihood is calculated for the H_{160} and J_{125} independently and summed to generate a total log-likelihood for a given model.

3.2 MCMC lens modelling

We run the MCMC code with the 10 parameters described above. The data are cropped WFC3 FITS files in J_{125} and H_{160} , along with oversampled PSFs and root mean square (RMS) maps. The code allows for oversampled PSFs by oversampling the image plane equivalently. The step size is optimised to deliver a success rate of 1/3. As is standard,

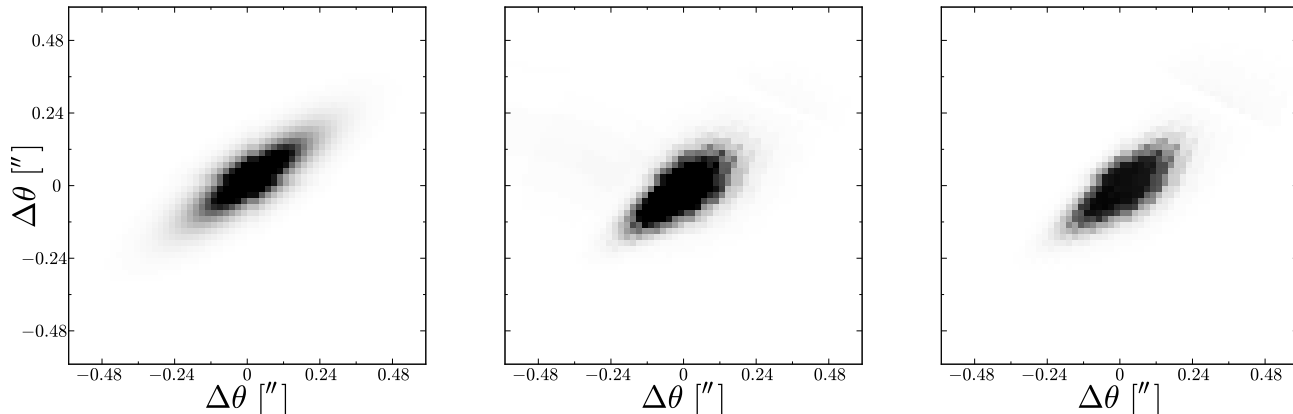


Figure 8. Left: The MCMC recovered source. Centre: the J_{125} LENSVIEW reconstruction. Right: the H_{160} LENSVIEW reconstruction. As gravitational lensing magnifies surface area while preserving surface brightness, spatial information of the source can be recovered with more detail than if it was not magnified. The source plane is sampled at a pixel scale 4 times finer than the data. These sources have not been convolved with the HST WFC3 PSF. All three panels are 1.2 arcsec on each side and shown on the same contrast scale.

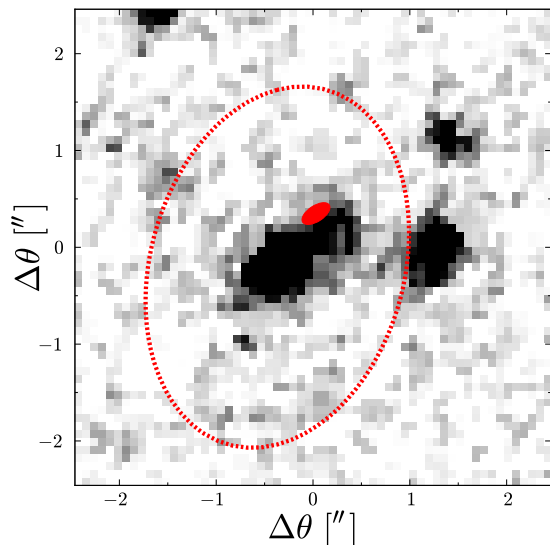


Figure 7. The lens model with parameters at the median of their MCMC distribution. The red filled ellipse represents the source position in this model, and is shown with its intrinsic orientation and ellipticity. More detailed reconstructions of the source are shown in Fig. 8. The critical curve is plotted (dashed red). This lens model accurately reproduces the positions of the primary and counter images. This model produces a flux ratio of 4.92 consistent with the observed value. The tangential elongation in the primary image along the critical curve is evident in this figure.

we discard the MCMC burn in. We find well-constrained posterior probability distribution functions (posterior PDF) for each source and lens parameter.

The inferred parameters from the MCMC analysis are presented in Table 2. A deflector with an Einstein radius of 1.49 ± 0.03 arcsec and ellipticity $\epsilon = 0.70^{+0.05}_{-0.11}$ at $-15.3^{+2.7}_{-2.0}$ ° East of North is favoured by the data. The source has a

Parameter	Posterior median
SIE θ_{ER}	1.49 ± 0.03 arcsec
SIE ellipticity	$0.31^{+0.03}_{-0.01}$
SIE position angle	$-15.3^{+2.7}_{-2.0}$ °
Source x-position	$0.39^{+0.02}_{-0.01}$ arcsec
Source y-position	0.54 ± 0.01 arcsec
Source flux	$0.20^{+0.03}_{-0.02}$ cps
Source ellipticity	$0.70^{+0.05}_{-0.11}$
Source position angle	$-57.0^{+2.8}_{-1.8}$ °
Source r_e	0.14 ± 0.01 arcsec
Source Sérsic index	$0.92^{+0.24}_{-0.16}$

Table 2. Posterior medians and 68 percent confidence intervals for the parameters of the deflector and source model. Uniform priors have been assumed for all parameters.

Sérsic index of $n = 0.92^{+0.24}_{-0.16}$ and a major-axis half-light radius of 0.7 ± 0.1 kpc (in Section 4 **SExtractor** is used to determine the circularised half-light radius for consistency with the literature). The apparent magnitude of the source would be $m_{J_{125}} = 27.5 \pm 0.1$ mag if observed without magnification. The magnification at the location of the primary image is $\mu = 4.3 \pm 0.2$. The total magnification is $\mu = 5.2 \pm 0.3$. The lens model based on the median of the posterior PDF of each parameter is presented in Fig. 7.

The source model is presented in the left panel of Fig. 8 at a finer pixel scale than the data as lensing allows the recovery of more spatial information than if the source was not lensed. The source is also reconstructed in the median lens model using LENSVIEW (Wayth & Webster 2006). LENSVIEW creates a mapping matrix for a given lens model which reverse maps image plane pixels to the source plane. This is done independently for the J_{125} and H_{160} images. The LENSVIEW reconstructions are shown in the centre and right panels of Figures 8 and agree well with the MCMC results.

This model predicts a flux ratio of the two images of 4.92, which is consistent with the observed value of 4.8 ± 2.6 . We did not impose an informative prior on the flux ratio, so all values are formally allowed in the model and deemed

equally likely. Hence, a consistent predicted flux ratio with the measured flux ratio in Section 2.4 supports the reality of the counter image at its observed location.

To investigate how constraining the marginal detection of the counter image is in the model, we run the MCMC code with the pixels at the location of the counter image masked. We find that in the absence of the counter image, the model is no longer well constrained and there is a degeneracy between the Einstein radius of the foreground galaxies, and the source position and magnification. This occurs because we place no informative priors on the Einstein radius and orientation of the foreground galaxies, hence massless galaxies and no magnification of the $z \sim 8$ LBG is considered equally as likely as intermediate or strong magnification of the source. In order to constrain the magnification of the source in the absence of the counter image, we place a prior on the velocity dispersion of the foreground galaxies using the Faber-Jackson relation of Barone-Nugent et al. (2015). Using this prior, we place a one sigma lower limit on the magnification of $\mu \geq 1.38$ when masking the counter image pixels.

4 SOURCE MORPHOLOGY

In this section we compare the predicted source parameters with other $z \sim 8$ galaxies from the literature. The intrinsic source profile recovered in our MCMC analysis, and independently using LENSVIEW on the J_{125} and H_{160} data, is presented in Fig. 8. We use SExtractor on the intrinsic sources to determine their intrinsic effective radii. The effective radius definition is not unique in the literature. For consistency with previous work on galaxy sizes at high redshift (Grazian et al. 2012) we use SExtractor to determine the effective radius, which uses concentric circular aperture measurements. In contrast, the effective radius value found in the MCMC analysis is defined along the major-axis of the Sérsic profile, which will vary by a factor of \sqrt{q} , where q is the axis ratio. The intrinsic effective radii of the source, recovered in the MCMC analysis and LENSVIEW, are presented in Table 3, and are consistent with the results of Oesch et al. (2009), who found the average intrinsic size of a $z \sim 8$ LBG to be ~ 0.5 kpc.

PSF broadening affects the measurement of effective radii. To first approximation,

$$r_e^{\text{obs}} = \sqrt{r_e^{\text{intr}2} + r_{\text{PSF}}^2} \quad (3)$$

where r_e^{obs} is the observed effective radius, r_e^{intr} is the intrinsic effective radius and r_{PSF} is the full width at half maximum of the PSF. Table 3 summarizes the measurements of the observed size.

We compare our results with the size-luminosity relation measured at $z \sim 7$ by Grazian et al. (2012) in Fig. 9. We account for an expected approximate scaling of the galaxy radius with redshift of $1/(1+z)$, in line with the study by Oesch et al. (2009) who constrained the redshift evolution of the scale-length of galactic disks in the HUDF, and theoretical predictions by Wyithe & Loeb (2011). We find that the recovered properties of our source are consistent with the

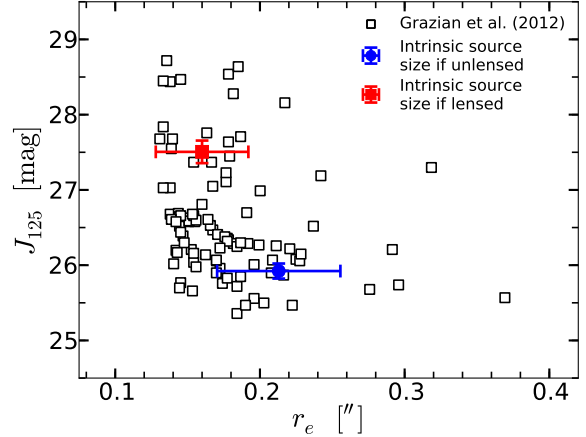


Figure 9. Size versus luminosity relation for the Y_{098} -dropout source under the lensing scenario, as recovered from our MCMC analysis and as reconstructed with LENSVIEW (red, $m_J = 27.5$ mag). The blue point ($m_J = 25.9$) shows the same measurement but assuming that no lensing magnification is present. Both scenarios are consistent with the size-luminosity relation measured by Grazian et al. (2012) at $z \sim 7$, and scaled to $z \sim 8$ assuming $r(z) \propto 1/(1+z)$ (Oesch et al. 2009; Wyithe & Loeb 2011). The change in distance modulus from $z = 7$ to $z = 8$ is accounted for.

$z \sim 7$ sample presented in that work. The LENSVIEW reconstruction and the source recovered in the MCMC analysis are plotted in red in Fig. 9. We also plot the size and luminosity of the primary image if it has not been lensed and find that the galaxy would not be an outlier on the relation.

Additionally, we compare our results with the size-luminosity relations of Shibuya et al. (2015) and Curtis-Lake et al. (2014). Shibuya et al. (2015) find the size of $\sim L_*$ LBGs at $z \sim 8$ to be $0.419_{-0.262}^{+1.981}$ kpc, consistent with the LBG if it has not been significantly magnified, and the size of LBGs two magnitudes fainter to be $0.243_{-0.068}^{+0.225}$ kpc, consistent with the size of the LBG under the strong lensing hypothesis. We also find that the size of the LBG under the lensing hypothesis is consistent with the sizes of the $z \sim 8$ LBGs in Curtis-Lake et al. (2014), but also consistent with the absence of lensing due to the scatter in the relation. Thus, the size of the Y_{098} -dropout is consistent with literature data whether the strong lensing hypothesis is true or not.

5 DEFLECTOR MASS-TO-LIGHT RATIO

Strong gravitational lensing offers a direct and uniquely precise measurement of the deflector mass distribution. Lensing constraints are free from assumptions of a system's dynamical properties which is critical in other direct measurements of a system's mass (Cappellari et al. 2009). Under the assumption that we are, in fact, observing a lensing system as described in this paper, we can measure the mass of a $z = 1.327$ group and its associated massive galaxies with unprecedented precision. We measure the mass enclosed within the Einstein radius of the deflector system, as well as the total mass enclosed within the effective radius of the brighter galaxy of the spectroscopically

Source	Angular r_e^{intr} [arcsec]	Proper r_e^{intr} [kpc]	Angular r_e^{obs} [arcsec]	Proper r_e^{obs} [kpc]
MCMC analysis	0.09 ± 0.02	0.45 ± 0.08	0.16 ± 0.03	0.80 ± 0.15
J_{125} LENSVIEW	0.10 ± 0.02	0.50 ± 0.09	0.16 ± 0.03	0.80 ± 0.15
H_{160} LENSVIEW	0.10 ± 0.02	0.50 ± 0.09	0.17 ± 0.03	0.85 ± 0.16

Table 3. The intrinsic and WFC3 observed effective radii of the source recovered in the multi-band MCMC analysis, and reconstructed independently for each band using LENSVIEW. The intrinsic values are the source sizes once corrected for PSF-broadening, while the observed sizes include the effect of PSF-broadening.

confirmed deflector.

To calculate the mass enclosed by the Einstein radius, we integrate the SIE mass distribution over the Einstein radius of 1.49 arcsec. We find the mass within the effective radius by fitting a de Vaucouleurs profile to the light from the main deflector galaxy using GALFIT in order to determine its effective radius, r_e . The mass within the effective radius is then calculated by integrating the SIE mass distribution over r_e . It should be noted that the effective radius of the de Vaucouleurs profile is defined by GALFIT along the major axis. For consistency with the mass measurement within the Einstein radius, we integrate the mass over the effective radius defined along the intermediate axis.

Calculating the physical masses and intrinsic luminosities of the deflector galaxies requires knowledge of the source and deflector redshifts. We consider the uncertainty in the spectroscopic redshift of the main deflector to be negligible compared to the uncertainty in the source LBG’s redshift, and other systematic errors. The non-negligible range for the redshift PDF of the source redshift is $7.6 \lesssim z \lesssim 8.8$, and the uncertainty on the brighter galaxy’s effective radius is approximated to be 20 per cent in order to account for systematic errors which dominate the formal statistical errors provided by GALFIT. The centre of the deflector is fixed in the MCMC analysis, but we account for uncertainty in its location when calculating the physical mass enclosed within the effective radius of the brighter galaxy. We also include errors on the solar luminosity, K correction, systematics in the photometry and random errors in the MCMC analysis. The resulting values for measured quantities are quoted at their median and the resulting errors on the derived quantities are quoted and plotted at the 68 per cent confidence limit.

The mass enclosed within the Einstein Radius of 1.49 arcsec of the SIE mass distribution is $(9.62 \pm 0.31) \times 10^{11} M_\odot$. Photometry of the luminous matter enclosed within the Einstein radius is listed in Table 1. We apply the distance modulus out to $z = 1.327$ and a K-correction using single stellar populations models with ages in the range 1-2 Gyr to convert the J_{125} magnitude to the rest-frame B -band magnitude. We note that the redshifted B band is very close to the observed J_{125} and therefore the K correction is fairly robust with respect to changes in the assumed spectral energy distribution, resulting in a negligible additional uncertainty. Combining these measurements, we find a total mass-to-light ratio within the Einstein radius of $M/L_B = 38.8_{-3.6}^{+4.2} M_\odot/L_\odot$. This suggests that dark matter dominates the mass of the deflector and supports the argument that the deflector is a group. The Einstein radius is ~ 20 times as large as the effective radius of the brighter deflector galaxy, which is consistent with a mass

distribution dominated by dark matter.

To obtain the stellar mass-to-light ratio of the brighter central deflector, we calculate the lensing mass within its effective radius and account for the dark matter fraction as follows. We use GALFIT to fit a de Vaucouleurs profile to the main deflector galaxy. We find it to have circularised $r_e = 0.072 \pm 0.014$ arcsec, and a magnitude of $m_{\text{deVauc}} = 23.55 \pm 0.1$ mag. We find the circular effective radius to be $0.62_{-0.13}^{+0.14}$ kpc, making the galaxy very compact and less luminous than the most massive galaxies at comparable redshift (Damjanov et al. 2009). Within this galaxy’s effective radius the SIE mass distribution has a mass of $4.3 \pm 0.3 \times 10^{10} M_\odot$. The left hand panel of Fig. 10 shows this galaxy’s stellar mass and effective radius in comparison with the sample of elliptical galaxies at $1 < z < 1.5$ from Newman et al. (2012).

We apply the distance modulus and K correction to convert the J_{125} magnitude to the rest-frame B -band magnitude. We find that the mass-to-light ratio within its effective radius is $M/L_B = 3.5_{-0.9}^{+1.2} M_\odot/L_\odot$. Adopting the average dark matter fraction of 1/3 found for SLACS systems of this mass (Treu & Koopmans 2004; Auger et al. 2010b), we obtain a stellar mass-to-light ratio of $M_*/L_B = 2.3_{-0.6}^{+0.8} M_\odot/L_\odot$. We find that the brighter deflecting galaxy is consistent in size and mass with compact, massive galaxies observed at similar redshifts (so-called ‘red nuggets’, Daddi et al. 2005; Van Dokkum et al. 2008; Damjanov et al. 2009; Newman et al. 2012). The right hand panel of Fig. 10 compares our measurement of the stellar mass-to-light ratio to previous measurements of the cosmic evolution of the stellar mass-to-light ratio obtained using lensing measurements at lower redshifts (Treu & Koopmans 2004) and via the evolution of the Fundamental Plane out to $z \sim 1.2$ (Treu et al. 2002).

6 DISCUSSION

In this paper, we have analysed what appears to be a case of strong gravitational lensing of a $z \sim 8$ LBG found in the BoRG survey. In the event that this source has been strongly lensed, we find the empirical strongly lensed fraction of LBGs detected at 8σ in BoRG to be 10 per cent. We discuss the supporting evidence for this hypothesis in this section.

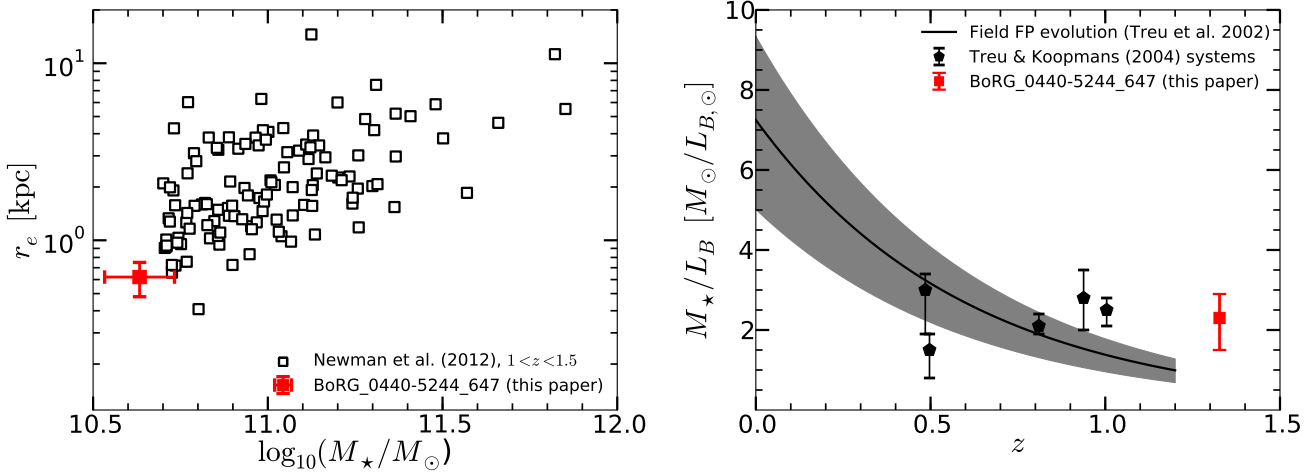


Figure 10. Left: The size mass relation at $1 < z < 1.5$. The open squares show the measured stellar masses from spectral synthesis models of multicolor photometry (Newman et al. 2012). Our lens candidate (red point) falls on the relation, using our lensing-based estimate of the stellar mass presented in this work. Right: Cosmic evolution of the stellar mass-to-light ratio based on gravitational lenses at lower redshift (Treu & Koopmans 2004), the evolution of the Fundamental Plane measured out to $z \sim 1.2$ (Treu et al. 2002). The red point represents the candidate lens presented in this paper.

6.1 Previous studies of the lensed fraction of high- z LBGs

The study of $z \sim 7-8$ LBGs in the XDF and CANDELS blank fields found the strongly lensed fraction of LBGs brighter than M_* to be ~ 6 per cent (Barone-Nugent et al. 2015). In a separate study by (Mason et al. 2015), the strongly lensed fraction in the BoRG fields is estimated at 3–15 per cent. These studies were based on the work by Wyithe et al. (2011), who predicted a strongly lensed fraction of 10 per cent for high redshift samples with a flux limit of $M < M_*$. These studies lead to the expectation that ≈ 1 of the 10 high-S/N LBGs, which are all approximately M_* or brighter, in the BoRG sample will show evidence for strong gravitational lensing.

6.2 Proximity to bright foreground objects

The $z \sim 8$ LBG we have identified as a good candidate for being strongly gravitationally lensed, borg_0440-5244.682, is observed in close proximity to multiple bright foreground objects, so there is a considerably enhanced chance of strong lensing for this LBG. Analysis of the CANDELS fields from Barone-Nugent et al. (2015) shows that random source positions observed within ~ 1.8 arcsec of a foreground galaxy with $M_B < -20$ mag have a greatly enhanced likelihood of being strong lensed over all random source positions. This analysis shows that the fraction of 50 000 random source positions found to be projected nearby to bright foreground objects is low (2 per cent of all random source positions are observed within 2.0 arcsec of a bright foreground galaxy). But of the 2 per cent which are projected within 2.0 arcsec, ~ 20 per cent will have been strongly gravitationally lensed.

Fig. 11 shows the likelihood of a random line of sight being observed within θ_{sep} of a foreground galaxy with $M_B < -20$ mag (solid black), and the likelihood of strong

lensing as a function of θ_{sep}^1 . An object being observed within 1.8 arcsec of a bright foreground objects implies that it has a 23 per cent chance of being strongly lensed. The probability of strong lensing is even more enhanced for objects observed around brighter objects (e.g. $M_B < -20.5$ mag), giving a likelihood of lensing of ~ 30 per cent at a separation of $\theta_{\text{sep}} = 1.8$ arcsec. The central galaxy pair (identified as a single foreground object), borg_0440-5244.647, has an absolute magnitude of $M_B = -20.5$ mag.

Bayes Theorem gives a similar result, where the likelihood of strong lensing (“SL”) given the observed separation between a high redshift object and a foreground object can be expressed as,

$$P(\text{SL}|\theta \leq 1''.8) = \frac{P(\theta \leq 1''.8|\text{SL})}{P(\theta \leq 1''.8)} P(\text{SL}) \quad (4)$$

where we can estimate values for $P(\text{SL})$ and $P(\theta \leq 1''.8|\text{SL})$ from fig. 4 of Barone-Nugent et al. (2015) and $P(\theta \leq 1''.8)$ from Fig. 11, and find that,

$$P(\text{SL}|\theta \leq 1''.8) \simeq \frac{0.6}{0.017} \times 0.008 \quad (5)$$

$$= 28\%. \quad (6)$$

6.3 The foreground objects are typical deflectors of $z \sim 8$ LBGs

In the study of gravitational lensing in the CANDELS fields by Barone-Nugent et al. (2015), they presented the empirical distribution of deflector luminosities, redshifts and deflector-source separations (see fig. 4 of Barone-Nugent et al. 2015). The spectroscopic redshift of the central foreground galaxy pair in this paper is consistent with the observed peak of

¹ This analysis is based on observations of the CANDELS fields using the methodology of Barone-Nugent et al. (2015).

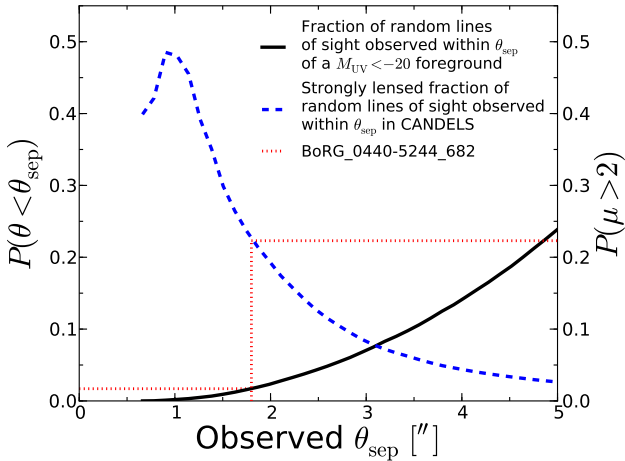


Figure 11. The probability of observing a random $z \sim 8$ source within θ_{sep} of a foreground galaxy with $M_B < -20$ mag (solid black), and the likelihood of strong lensing, $P(\mu > 2)$, of random lines of sight observed within θ_{sep} of a foreground galaxy with $M_B < -20$ mag (dashed blue) in the CANDELS fields using the model of Barone-Nugent et al. (2015). The red dotted lines mark the observed separation between borg_0440-5244.682 and borg_0440-5244.647 (1.8 arcsec). The likelihood of this random alignment is ~ 1.7 per cent, and the likelihood of strong lensing is ~ 23 per cent.

the redshift distribution for gravitational lenses of $z \sim 7-8$ LBGs, which occurs between $z \sim 1-2$. The observed separation between the central foreground objects and the $z \sim 8$ LBG candidate, $\theta_{\text{sep}} = 1.8$ arcsec, is also at the peak of the deflector-source separation distribution, which peaks at $1.5 < \theta_{\text{sep}} < 2.0$ arcsec. The luminosity of the central object is also near the peak of the absolute magnitude distribution. Additionally, the required Einstein radius derived in Section 3 of ~ 1.5 arcsec is consistent with strong lensing by a massive galaxy/group at moderate redshift (Treu & Koopmans 2002; Treu 2010; Newman et al. 2015).

Further to the point of the objects borg_0440-5244.647 and borg_0440-5244.650 being in the range of luminosities of gravitational deflectors in the CANDELS fields identified by Barone-Nugent et al. (2015), we can also infer the mass of these galaxies using abundance matching. Based on modelling of the galaxy luminosity function at high redshift (Trenti et al. 2014), abundance matching of the luminosity of the object borg_0440-5244.647 translates to an halo mass of $\sim 5.7 \times 10^{12} M_{\odot}$. The object borg_0440-5244.650's luminosity translates to a halo mass of $\sim 1.0 \times 10^{12} M_{\odot}$ if it is also at $z \sim 1.3$.

Associating these masses with the virial mass, and circular velocities with the virial velocity, this mass would give circular velocities $V_c \sim 270 \text{ kms}^{-1}$ and $V_c \sim 150 \text{ kms}^{-1}$ for the halos of the two galaxies borg_0440-5244.647 and borg_0440-5244.650, respectively. Translating circular velocities into central stellar velocity dispersions σ_* of an isothermal model for the deflector is complicated by baryonic physics which generally tend to increase the central velocity dispersion of a collapsed Navarro et al. (1997) dark matter halo. In practice, the circular velocity is comparable to the observed stellar velocity dispersion $\sigma_* \approx V_c$ at the

scale considered here (e.g., Bundy et al. 2007; Dutton et al. 2010), which in turn is very close to the velocity dispersion of the singular isothermal sphere that describes the total mass density profile in the inner regions of massive elliptical galaxies (Treu & Koopmans 2004; Koopmans et al. 2009; Auger et al. 2010a). In addition, the gravitational lensing optical depth is a strongly rising function of velocity dispersion (e.g. Ruff et al. 2011) and $\sigma_* \approx 300 \text{ kms}^{-1}$ is a typical value for group-sized halos (Treu & Koopmans 2002). These inferred velocity dispersions are sufficient to produce an Einstein radius of the magnitude required in Section 3.

6.4 Possible multiple imaging

Multiple imaging by a deflector is a necessary condition for strong lensing, although secondary images of the source will appear much fainter and closer to the deflector galaxy, making them difficult to detect at high significance (Wyithe et al. 2011; Fialkov & Loeb 2015). Consistent with this, we observe a possible faint counter image on the opposite side of the central deflector objects. Both the brighter image and the fainter image are completely absent in the Y_{098} and V_{600} filters, consistent with the $z \sim 8$ LBG selection criteria, and with the lensing hypothesis, as gravitational lensing is achromatic. The colours of the counter image are consistent with both the Y_{098} -dropout, and being a $z \sim 8$ object below the flux limit of the BoRG field. The observed flux ratio between the two images is consistent with the flux ratio predicted in the best fitting model in our lens modelling.

As discussed in Section 2.4, the counter image is not detected in the H_{160} image. This is expected based on the colours of the source and the sensitivity of the H_{160} and J_{125} images.

6.5 Elongation of the dropout

The $z \sim 8$ LBG is consistent with being elongated tangentially to the direction to the central foreground galaxies. In gravitational lensing theory, images are elongated into arcs and arclets along the critical curves of deflectors. Unless the deflector has very high ellipticity, the image's elongation will always be tangential to the direction from the image to the deflector. As described in Section 2.3, the primary image shows elongation that is tangential to the direction towards the central foreground galaxies with an ellipticity of $\epsilon = 0.4 \pm 0.1$. Our modelling of the system confirms that the observed elongation is consistent with that predicted by the model once smearing by the WFC3 PSF and low S/N of the data are taken into account.

6.6 Lack of companion dropouts in the field

Finally, we note that the field contains only this single candidate detected at high S/N. Based on dark matter (DM) clustering, we expect additional dropouts in the field if the primary image is not strongly magnified. Abundance matching predicts that the dropout is hosted in a rare dark matter halo with $M_{\text{DM}} \gtrsim 2 \times 10^{11} M_{\odot}$ (Muñoz & Loeb

2008; Trenti et al. 2012). However, the connection between DM halo mass and galaxy luminosity seems unclear at high redshift, as highlighted by the recent measurement of the two-point correlation function at $z \gtrsim 7$ from CANDELS and XDF catalogs (Barone-Nugent et al. 2014) and by the lack of strong clustering around a more luminous and isolated galaxy at $z = 7.7$ (Oesch et al. 2015). Therefore, while the lensing hypothesis provides a natural explanation of this single bright candidate (the dropout would be intrinsically fainter and hence less clustered), further studies are needed to use the lack of clustering as a quantitative support for the lensing hypothesis.

6.7 Comparison with previous lensing studies of the BoRG sample

The configuration we have investigated in this paper was not identified in the analysis of Mason et al. (2015) as a strong lensing candidate. Based on a Faber-Jackson relation (Faber & Jackson 1976), Mason et al. (2015) only identified a single different object from our high S/N sample as a candidate for being gravitationally magnified by a foreground object (inferring a magnification for that object of $\mu = 1.47 \pm 0.3$). However, there are a number of reasons that the galaxy we have identified in this paper was missed by Mason et al. (2015). Firstly, we have obtained additional spectroscopy which places the nearby objects at a lower redshift than the photometric redshift used in the Mason et al. (2015) analysis, which leads to a lower required mass for strong gravitational lensing. Secondly, the Faber-Jackson relation used by Mason et al. (2015) will underestimate the lensing potential of a gravitational deflector which consists of multiple objects, because gravitational magnification is not linearly additive (Wong et al. 2012) and much more dark matter is expected in group environments.

We find that when the central foreground galaxy pair, which is identified as a single object in the BoRG catalogue, is considered at its correct redshift, the estimated magnification of borg_0440-5244.682 in the Mason et al. (2015) framework increases by ~ 10 per cent to $\mu = 1.41$. We also infer the magnification with velocity dispersions found using the Faber-Jackson relation of Barone-Nugent et al. (2015) and their lensing likelihood framework, which leads to the estimated magnification of borg_0440-5244.682 to be $\mu = 1.47^{+0.30}_{-0.18}$, and a strong lensing likelihood of 11 per cent.

If the object borg_0440-5244.650 also resides at $z = 1.3$ and is included as a third deflector, the magnification further increases at the location of the dropout. In fact, when including this third lensing galaxy at $z \simeq 1.3$ and using the velocity dispersions inferred from the FJR of Barone-Nugent et al. (2015), the magnification at the location of the dropout is $\mu = 1.96^{+0.63}_{-0.36}$, giving it a strong lensing likelihood of 47 per cent.

The case presented in this paper highlights that the available photometry of both the source LBG and the photometric and spectroscopic observations of the foreground group, and the inferences on the group's mass, are completely consistent with this configuration resulting in a high magnification of the $z \sim 8$ LBG. In fact, the

foreground group would need a peculiarly low mass given its luminosity for there to be low magnification ($\mu \lesssim 1.4$) of the LBG.

7 CONCLUSION

In this paper, we use broad-band HST photometry to identify a candidate galaxy-scale gravitational lensing system composed of a $z \sim 8$ LBG source and a small foreground group. To follow-up the system we have obtained very deep VLT/X-Shooter spectroscopy of the LBG and two members of the group. Our new spectroscopic data confirm that the foreground galaxy pair has a redshift of $z = 1.327$ through detection of multiple emission lines. A third possible foreground deflector galaxy, not targeted by spectroscopy, has an extended photometric redshift distribution, with a non-negligible likelihood around $z = 1.3$. The X-Shooter spectroscopy also allows us to exclude the LBG candidate as a low-redshift interloper with strong emission lines with high confidence (70σ in H_{160}). Therefore, due to the small angular separation between the LBG and the foreground galaxies, the foreground galaxy pair's spectroscopic redshift and the ruling out of lower redshift solutions for the LBG from the absence of emission lines, the dropout must have been gravitationally magnified to some degree. In this paper, we carried out a detailed modelling with the goal of quantifying the magnification. We argue that the most likely configuration is that the $z \sim 8$ source has been magnified by $\mu = 4.3 \pm 0.2$, producing a secondary demagnified image on the opposite side of the deflector galaxies. We marginally detect this secondary image (with $S/N \sim 2$) in the band with the deepest imaging, J_{125} .

The lens model yields a total group mass of $9.62 \pm 0.31 \times 10^{11} M_{\odot}$, which is very close to the mass expected from abundance matching. We have obtained a lensing measurement of the stellar mass of a compact galaxy at $z = 1.327$, without being affected by the systematic uncertainties that are associated with the inference of stellar mass from spectral energy distribution using population synthesis models. Assuming the standard dark matter fraction found for lower redshift lenses, the brighter central deflector galaxy has a stellar mass-to-light ratio of $M_{\star}/L_B = 2.3^{+0.8}_{-0.6} M_{\odot}/L_{\odot}$ within its effective radius. Overall, the properties of the main lensing galaxy are consistent with observations of 'red nuggets' at similar redshifts (Daddi et al. 2005; Trujillo et al. 2006; Buitrago et al. 2008; Van Dokkum et al. 2008). This represents a leap forward compared to other similar measurements from gravitational lensing, which are limited to $z \lesssim 1$ (see Fig. 10).

Using this interpretation of the data, we find a strongly lensed fraction of galaxies bright than $\approx M_{\star}$ in BoRG to be 10 per cent. While the uncertainty on this number is large due to the rarity of bright $z \sim 8$ objects, this value is quantitatively consistent with the findings of Mason et al. (2015), who found an expected strongly lensed fraction of 3 – 15 per cent in the BoRG fields, the recent analysis of the CANDELS fields and the XDF by Barone-Nugent et al. (2015) and theoretical modelling by Wyithe et al. (2011). Since Wyithe et al. (2011) showed that the effect

of magnification bias on the galaxy luminosity function increases with redshift, quantifying and verifying its impact at $z \sim 8$ is important for predictions for future surveys targeted at finding $L \gtrsim L_*$ galaxies at yet higher redshift, such as *Euclid* and surveys using *JWST* and *WFIRST*.

Overall, the strong lensing configuration derived by our work is the most natural interpretation, but a more precise measurement of the magnification of the source and the counter image would allow more robust inferences about the system. Intriguingly, our modelling makes specific predictions testable with deeper HST imaging, including the precise flux ratio between the two images and the elongation of the brighter image. Improving the S/N of the observations by a factor of two would allow both these measurements and hence allow a better determination of the magnification of this $z \sim 8$ LBG. Such a goal is within reach of HST as it would require only ~ 10 orbits of observations.

Acknowledgments This work is partially supported by programs number HST/GO 11700, 12587, 12905, and 13767 from NASA through a grant from the Space Telescope Science Institute, which is operated by the Association of Universities for Research in Astronomy, Inc, under NASA contract NAS5-26555. JSBW acknowledges the support of an Australian Research Council Laureate Fellowship. MT acknowledges the support of an Australia Research Council Future Fellowship. We would like to acknowledge the anonymous referee for their helpful comments, Sharon Rapoport for her initial lens modelling of the system and Stephanie Bernard for her help with the BoRG data.

REFERENCES

- Ade P. et al., 2013, arXiv preprint arXiv:1303.5062
- Alard C., 2000, *Astronomy and Astrophysics Supplement Series*, 144, 363
- Atek H. et al., 2011, *The Astrophysical Journal*, 743, 121
- Auger M., Treu T., Bolton A., Gavazzi R., Koopmans L., Marshall P., Moustakas L., Burles S., 2010a, *The Astrophysical Journal*, 724, 511
- Auger M., Treu T., Gavazzi R., Bolton A., Koopmans L., Marshall P., 2010b, *The Astrophysical Journal Letters*, 721, L163
- Barkana R., Loeb A., 2000, *The Astrophysical Journal*, 531, 613
- Barone-Nugent R. et al., 2014, *The Astrophysical Journal*, 793, 17
- Barone-Nugent R., Wyithe J., Trenti M., Treu T., Oesch P., Bouwens R., Schmidt K. B., 2015, *Monthly Notices of the Royal Astronomical Society*
- Benitez N., 2000, *The Astrophysical Journal*, 536, 571
- Benitez N., 2008, *The Astrophysical Journal*, 536, 571
- Benítez N. et al., 2004, *The Astrophysical Journal Supplement Series*, 150, 1
- Bouwens R. et al., 2011, *The Astrophysical Journal*, 737, 90
- Bouwens R. et al., 2015, *The Astrophysical Journal*, 803, 34
- Bouwens R. J., Illingworth G. D., Franx M., Ford H., 2008, *The Astrophysical Journal*, 686, 230
- Bradley L. et al., 2012, *The Astrophysical Journal*, 760, 108
- Buitrago F., Trujillo I., Conselice C. J., Bouwens R. J., Dickinson M., Yan H., 2008, *The Astrophysical Journal Letters*, 687, L61
- Bundy K., Treu T., Ellis R. S., 2007, *The Astrophysical Journal Letters*, 665, L5
- Cappellari M. et al., 2009, *The Astrophysical Journal Letters*, 704, L34
- Castellano M. et al., 2010, arXiv preprint arXiv:1007.5396
- Coe D., Benítez N., Sánchez S., Jee M., Bouwens R., Ford H., 2007, *The Astronomical Journal*, 132, 926
- Comerford J. M., Haiman Z., Schaye J., 2002, *The Astrophysical Journal*, 580, 63
- Curtis-Lake E. et al., 2014, arXiv preprint arXiv:1409.1832
- Daddi E. et al., 2005, *The Astrophysical Journal*, 626, 680
- Damjanov I. et al., 2009, *The Astrophysical Journal*, 695, 101
- Dutton A. A., Conroy C., van den Bosch F. C., Prada F., More S., 2010, *Monthly Notices of the Royal Astronomical Society*, 407, 2
- Faber S., Jackson R. E., 1976, *The Astrophysical Journal*, 204, 668
- Fialkov A., Loeb A., 2015, arXiv preprint arXiv:1502.03141
- Finkelstein S. et al., 2013, *Nature*, 502, 524
- Finkelstein S. L. et al., 2012, *The Astrophysical Journal*, 758, 93
- Finkelstein S. L. et al., 2014, arXiv preprint arXiv:1410.5439
- Giavalisco M., 2002, *Annual Review of Astronomy and Astrophysics*, 40, 579
- Grazian A. et al., 2012, *Astronomy & Astrophysics*
- Grogin N. A. et al., 2011, *The Astrophysical Journal Supplement Series*, 197, 35
- Illingworth G. et al., 2013, *The Astrophysical Journal Supplement Series*, 209, 6
- Keeton C., 2001a, arXiv preprint astro-ph/0102341
- Keeton C., 2001b, arXiv preprint astro-ph/0102340
- Khochfar S., Silk J., Windhorst R., Ryan Jr R., 2007, *The Astrophysical Journal Letters*, 668, L115
- Kochanek C. S., 1995, *The Astrophysical Journal*, 445, 559
- Koekemoer A. M. et al., 2011, *The Astrophysical Journal Supplement Series*, 197, 36
- Komatsu E. et al., 2010, arXiv preprint arXiv:1001.4538
- Koopmans L. et al., 2009, *The Astrophysical Journal Letters*, 703, L51
- Mason C. et al., 2015
- McLure R. et al., 2013, *Monthly Notices of the Royal Astronomical Society*, stt627
- Modigliani A. et al., 2010, in *SPIE Astronomical Telescopes+ Instrumentation*, International Society for Optics and Photonics, pp. 773728–773728
- Muñoz J. A., Loeb A., 2008, *Monthly Notices of the Royal Astronomical Society*, 385, 2175
- Navarro J. F., Frenk C. S., White S. D., 1997, *The Astrophysical Journal*, 490, 493
- Newman A. B., Ellis R. S., Bundy K., Treu T., 2012, *The Astrophysical Journal*, 746, 162
- Newman A. B., Ellis R. S., Treu T., 2015, arXiv preprint arXiv:1503.05282
- Oesch P. et al., 2009, *The Astrophysical Journal Letters*, 709, L21

- Oesch P. et al., 2012, *The Astrophysical Journal*, 759, 135
- Oesch P. et al., 2015, arXiv preprint arXiv:1502.05399
- Oke J., Gunn J., 1983, *The Astrophysical Journal*, 266, 713
- Ono Y. et al., 2011, *The Astrophysical Journal*, 744, 83
- Robertson B. E., Ellis R. S., Furlanetto S. R., Dunlop J. S., 2015, *The Astrophysical Journal Letters*, 802, L19
- Robertson B. E. et al., 2013, *The Astrophysical Journal*, 768, 71
- Ruff A., Gavazzi R., Marshall P., Treu T., Auger M., Brault F., 2011, *The Astrophysical Journal*, 727, 96
- Schenker M. A. et al., 2013, *The Astrophysical Journal*, 768, 196
- Schmidt K. B. et al., 2014, *The Astrophysical Journal*, 786, 196
- Sérsic J., 1963, *Boletín de la Asociación Argentina de Astronomía La Plata Argentina*, 6, 41
- Shibuya T., Ouchi M., Harikane Y., 2015, arXiv preprint arXiv:1503.07481
- Shull J., Harness A., Trenti M., Smith B., 2012, *The Astrophysical Journal*, 747, 100
- Stark D. P. et al., 2015a, *Monthly Notices of the Royal Astronomical Society*, 450, 1846
- Stark D. P. et al., 2015b, arXiv preprint arXiv:1504.06881
- Steidel C., Giavalisco M., Dickinson M., Adelberger K., 1996, Arxiv preprint astro-ph/9604140
- Trenti M. et al., 2011, *The Astrophysical Journal Letters*, 727, L39
- Trenti M. et al., 2012, *The Astrophysical Journal*, 746, 55
- Trenti M., Perna R., Jimenez R., 2014, arXiv preprint arXiv:1406.1503
- Trenti M., Smith B. D., Hallman E. J., Skillman S. W., Shull J. M., 2010, *The Astrophysical Journal*, 711, 1198
- Trenti M., Stiavelli M., 2008, *The Astrophysical Journal*, 676, 767
- Treu T., 2010, *Annual Review of Astronomy and Astrophysics*, 48, 87
- Treu T., Koopmans L., 2002, *The Astrophysical Journal*, 575, 87
- Treu T., Koopmans L. V. E., 2004, *The Astrophysical Journal*, 611, 739
- Treu T., Schmidt K. B., Trenti M., Bradley L. D., Stiavelli M., 2013, arXiv preprint arXiv:1308.5985
- Treu T., Stiavelli M., Casertano S., Møller P., Bertin G., 2002, *The Astrophysical Journal Letters*, 564, L13
- Trujillo I. et al., 2006, *Monthly Notices of the Royal Astronomical Society: Letters*, 373, L36
- Van Dokkum P. G. et al., 2008, *The Astrophysical Journal Letters*, 677, L5
- Wallington S., Narayan R., 1993, *The Astrophysical Journal*, 403, 517
- Wayth R., Webster R., 2006, *Monthly Notices of the Royal Astronomical Society*, 372, 1187
- Wong K. C., Ammons S. M., Keeton C. R., Zabludoff A. I., 2012, *The Astrophysical Journal*, 752, 104
- Wong K. C. et al., 2014, *The Astrophysical Journal Letters*, 789, L31
- Wyithe J., Yan H., Windhorst R., Mao S., 2011, *Nature*, 469, 181
- Wyithe J. S. B., Loeb A., 2011, *Monthly Notices of the Royal Astronomical Society: Letters*, 413, L38
- Yan H. et al., 2011, *The Astrophysical Journal Letters*, 728, L22